Heliyon 10 (2024) e38107

Contents lists available at ScienceDirect

Heliyon

journal homepage: www.cell.com/heliyon

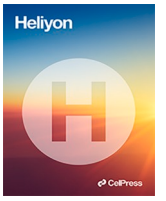

Research article

A 3D printed serrated contact structure triboelectric nanogenerator for swimming training safety monitoring

Xiao Liang [a], Jie Gao [b], Wei Wen [b,*]

[a] Sports Department, Capital University of Economics and Business, Beijing, 100070, China
[b] China Swimming College, Beijing Sport University, Beijing, 100091, China

ARTICLE INFO

Keywords:
Triboelectric nanogenerators (TENGs)
3D printing technology
Serrated contact structure
Intelligence sports
Swimming safety monitoring

ABSTRACT

The wearable electronic devices integrated with 3D printing have attracted much attention, but the continuous power supply demand and limited application scenarios have limited their development. Here, we propose a 3D printed serrated contact structure triboelectric nanogenerator (S-TENG) designed for mechanical energy harvesting and swimming training safety monitoring. Leveraging the advancements in 3D printing technology, we created a flexible, lightweight sensor integrated with polytetrafluoroethylene (PTFE) and polyethylene terephthalate (PET) films on a serrated substrate. This configuration enhances the contact surface area, leading to a significant improvement in energy harvesting efficiency compared to flat structures. Specifically, the serrated structure resulted in a 64 %, 63 %, and 47 % increase in open-circuit voltage (V_{oc}), short-circuit current (I_{sc}), and transferred charge (Q_{sc}), respectively, owing to the contact area and unique surface functional structure. The S-TENG device exhibits excellent performance under various bending angles, with V_{oc}, I_{sc}, and Q_{sc} reaching up to 98.04 V, 4.35 μA, and 38.51 nC at 90° bending. Additionally, the S-TENG maintains stable output in different humidity environments due to its fully encapsulated design, ensuring reliable operation in aquatic settings. The S-TENG can accurately measure elbow swing amplitude and frequency, providing valuable real-time data for athletes and coaches. The S-TENG's ability to detect irregular movements and potential drowning incidents underscores its promise in enhancing swimmer safety. This research demonstrates the S-TENG's utility in both energy harvesting and motion monitoring, paving the way for advanced wearable sports sensors in various athletic disciplines.

1. Introduction

Recently, with the rapid development of wearable technology and the Internet of Things (IoTs), intelligent motion monitoring has become an important catalyst for the advancement of the sports industry [1,2]. The integration of IoTs technology significantly enhances the capabilities of intelligent motion monitoring by facilitating seamless communication between multiple devices and sensors, thereby enabling more comprehensive data collection and analysis [3]. Intelligent motion monitoring requires numerous advanced wearable sensors to achieve effective recognition of various technological movements [4,5]. IoTs's connectivity allows these sensors to work in unison, creating a distributed sensor network that can effectively collect and transmit diverse motion information, including

* Corresponding author.
E-mail address: 2461@bsu.edu.cn (W. Wen).

https://doi.org/10.1016/j.heliyon.2024.e38107
Received 19 June 2024; Received in revised form 12 September 2024; Accepted 18 September 2024
Available online 18 September 2024

strength, speed, and posture. This network not only quantifies the movement behavior and kinematic patterns of athletes but also aids in improving their skills, developing scientific training plans, and formulating competition strategies [6]. Accurate motion recognition and real-time feedback are particularly crucial in swimming training and safety monitoring, where IoTs-enabled sensors can provide continuous updates and alerts [7]. However, traditional sensors depend on external power sources and face challenges such as inflexibility, complex wiring, and high battery replacement costs, making them unsuitable for large-scale applications. Triboelectric nanogenerators (TENGs) emerge as a sustainable self-powered alternative due to their simple structure [8–14], flexible material selection [15,16], and low-cost [17–19]. Since TENG was first proposed in 2012, sensors based on triboelectric technology have been widely used in human pose recognition [20,21], pressure sensing [22–24], and vibration detection [25,26], showing great potential in the field of intelligent motion. In swimming monitoring, TENG can not only provide exercise data but also contribute to safety monitoring by detecting abnormal exercise patterns to prevent drowning accidents [27]. Moreover, TENG has demonstrated outstanding performance in developing wearable sports sensors, when combined with IoTs, can be widely applied to various sports [28,29]. The triboelectric sensors provide continuous and real-time sports data, assisting in scientific training and enhancing sports safety. The synergy between TENG technology and IoTs not only advances the functionality of wearable sports sensors but also promotes a more connected and responsive sports monitoring ecosystem. Hence, developing TENG with wearable functions is promising, especially in the intelligent sports field.

The development of folded [30,31], arched [32–34], textile-based [35,36], and hydrogel-based [37–39] structures has significantly advanced the field of wearable TENGs. Folded and arched structures improve mechanical deformation capabilities and energy harvesting efficiency. Textile-based TENGs offer seamless integration with clothing, providing comfort and continuous energy harvesting from natural movements. Hydrogel-based TENGs bring high flexibility and suitability for wet environments, expanding the potential applications of wearable TENGs. However, these structural designs also present common challenges related to durability, environmental sensitivity, manufacturing complexity, mechanical and electrical stability, and integration with electronics. Addressing these drawbacks is crucial for advancing the practical application and widespread adoption of wearable TENGs in various fields, including sports monitoring [40], healthcare [41], and personal electronics [42–44]. Future research should focus on developing materials and designs that enhance the robustness and reliability of TENGs while maintaining their advanced functionalities. Considering the special requirement of minimizing interference to human movement in motion monitoring, wearable sensors must be flexible and lightweight. Therefore, currently, TENG based flexible sensors are mainly integrated with multi-layer thin films. 3D printing technology offers significant advantages in flexible wearable sports monitoring TENG [45]. It can precisely print sensors that conform to the human body or sports facilities, improving measurement accuracy and comfort [46]. The technology enables quick customization of TENG sensors to fit various sports, enhancing production efficiency and reducing costs [47]. Unlike traditional film-based sensors, 3D printing can create sensors with complex shapes that adhere well to 3D surfaces, improving adhesion and stability [48,49]. In swimming, 3D printed TENG sensors can be tailored to fit swimsuits or caps, maintaining performance underwater. This technology effectively meets the need for flexible, customized sensors in various motion environments. Besides, TENG based on sawtooth shaped structure can be used to obtain more human motion information. For example, Wang et al. proposed a serrated sandwich structure with promising applications in monitoring human race walk [50]. Furthermore, Wang reported a flexible serrated structure for joint monitoring in basketball sports [51]. Therefore, by combining 3D printing technology, TENG-based serrated structure will be able to better adapt to various complex motion monitoring needs, promote the development of intelligent motion monitoring, and provide more effective technical support for scientific training and motion safety.

Herein, we proposed a serrated contact structure triboelectric nanogenerator (S-TENG) by utilizing 3D printing technology for obtaining mechanical energy and swimming training safety monitoring. The polytetrafluoroethylene (PTFE) film and polyethylene terephthalate (PET) film are mounted on the flexible substrate with the serrated structure as triboelectric pair. The flexible 3D printing substrate endows the triboelectric layer with more flexible and sufficient triboelectric contact. Accordingly, the contact structure endows S-TENG with efficient energy harvesting efficiency. Compared to the flat structure, the serrated structure resulted in a 64 %, 63 %, and 47 % improvement in performance indicators such as open-circuit voltage (V_{oc}), short-circuit current (I_{sc}), and transfer charge (Q_{sc}) for S-TENG. Also, the serrated contact structure provides S-TENG with the ability to work under bending deformation. According to results, the V_{oc}, I_{sc}, and Q_{sc} of S-TENG increases with the bending angle, reaching up to 98.04 V, 4.35 μA, and 38.51 nC at 90°. By packaging the devices, S-TENG can achieve stable output in different humidity environments, which provides a foundation for its application in swimming monitoring. This feature highlights the S-TENG's ability to improve swimmer safety by offering early distress warnings. Using S-TENG for swimming monitoring introduces a new method for tracking and boosting swimmer performance. The S-TENG device precisely measures elbow swing amplitude and frequency, delivering valuable information for athletes and coaches. Moreover, the S-TENG's capacity to identify irregular movements and potential drowning incidents underscores its promise in safety applications.

2. Experiments

2.1. Materials

The base materials used for constructing the device were flexible substrates, aluminum, polyethylene terephthalate (PET), and polytetrafluoroethylene (PTFE). The substrates were produced using a 3D printing technique, ensuring precise and customizable geometries essential for the device's performance. The initial substrate was fabricated using a 3D printer, which provided a flexible and robust foundation. The aluminum layer was adhered to the substrate to serve as the conductive electrode. PET and PTFE were chosen for their triboelectric properties, which are critical for the device's functionality.

2.2. Characterization and measurements

The V_{oc} of S-TENG was measured using a Tektronix TDS 2024C digital oscilloscope. The S-TENG device was connected to the oscilloscope using shielded cables to minimize electrical noise. The sampling rate of the oscilloscope was set to 10 kHz to capture transient voltage spikes accurately. Measurements were taken under controlled environmental conditions (temperature: 25 °C, humidity: 50 %) to ensure consistency. The Q_{sc} and I_{sc} of S-TENG were measured using a Keithley 6514 electrometer. The electrometer was configured to the most sensitive range to detect low-level currents and charges generated by the S-TENG device. A custom-built mechanical system was employed to apply consistent force to the S-TENG device. The system was capable of controlling both the frequency and amplitude of the applied force. All tests were conducted in an enclosure to prevent external vibrations or airflow from affecting the results. Raw data collected from the oscilloscope and electrometer were processed using MATLAB. A low-pass filter was applied to the voltage and current data to remove high-frequency noise components. To thoroughly analyze the surface characteristics of the S-TENG, a scanning electron microscope (SEM), specifically a Hitachi SU7000, was utilized. This flexibility is primarily due to the use of a 3D printed substrate, which was fabricated using a high-precision 3D printer (e.g., Tuozhu P1SC) equipped with a flexible resin. For the performance evaluation of the S-TENG, a custom-built mechanical system was employed to provide controlled, repetitive mechanical stimuli to the device, simulating real-world operational conditions. This system is capable of supplying continuous power to the S-TENG, ensuring consistent testing parameters. The V_{oc} generated by the S-TENG was recorded using a high-resolution digital oscilloscope (e.g., DSOX1204G), which captures the voltage output with precision. Additionally, the Q_{sc} and I_{sc} were measured using a sensitive electrometer (Keithley 6514). The electrometer was calibrated before each set of measurements to ensure accuracy, and all data were recorded in a controlled environment to minimize the effects of external variables. The ambient temperature and humidity during testing, were meticulously controlled by digital temperature and humidity controller (WSK-Z (TH).

3. Results and discussion

3.1. The fabrication process of S-TENG device

The fabrication process of the S-TENG device, as illustrated in Fig. 1(a–d), involves multiple steps utilizing 3D printed flexible substrates. The process begins with the preparation of two separate components, each based on a flexible substrate produced through 3D printing. For the first component, as outlined in Fig. 1(a), the construction starts with the substrate (Fig. 1(a1)). A layer of aluminum is carefully aligned and adhered to this flexible substrate, ensuring that there is no air gap between the aluminum and the substrate to maintain uniform contact (Fig. 1(a2)). The adhesion process might involve applying a slight pressure or using a roller to

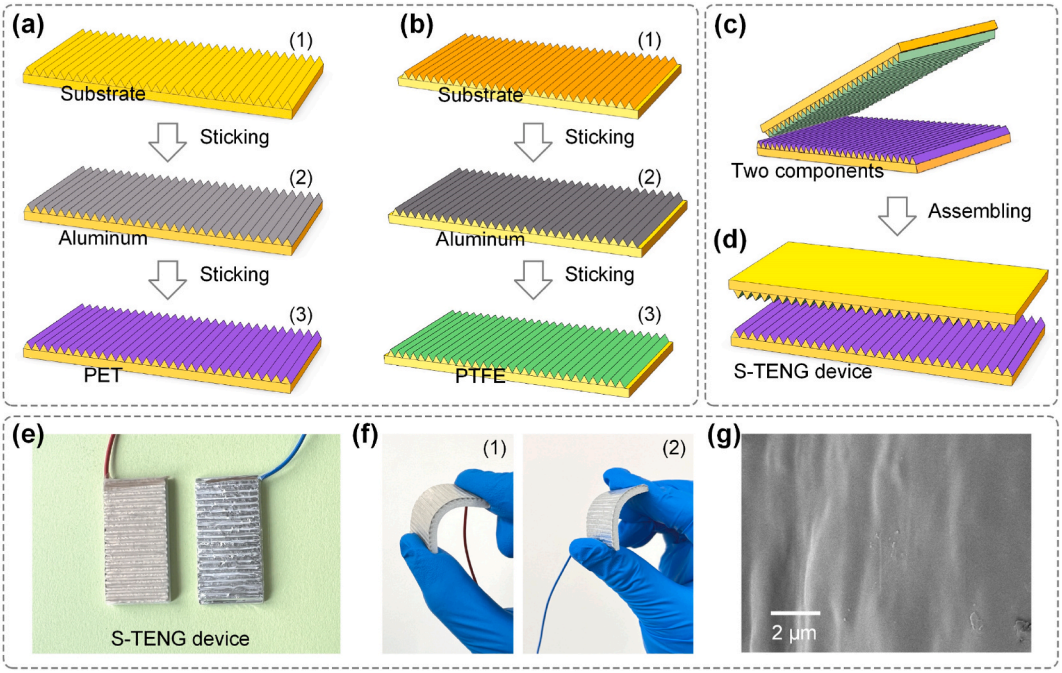

Fig. 1. The construction process of the (a1-a3) first component and (b1-b3) second component for S-TENG device fabrication. (c) The assembly process of two components for S-TENG device fabrication. (d) The structural diagram of S-TENG device, where the triboelectric layers are sandwiched between the flexible substrates. (e) The completed S-TENG device picture, shown with electrical connections for electrical output. (f1, f2) Demonstration of the device's flexibility, highlighting its ability to bend in multiple orientations without compromising structural integrity. (g) The SEM image showing the detailed surface morphology of the PTFE layer.

smooth out any wrinkles or bubbles that could form during the sticking process. Following this, a PET (polyethylene terephthalate) film is carefully placed on top of the aluminum layer (Fig. 1(a3)). This PET layer acts as a triboelectric material, and special attention is given to ensure that the film is uniformly attached, possibly involving a heating or pressing step to secure it firmly. The second component, illustrated in Fig. 1(b), follows a similar construction method. Starting with the 3D printed flexible substrate (Fig. 1(b1)), a layer of aluminum is attached in the same meticulous manner as described for the first component (Fig. 1(b2)). After ensuring that the aluminum layer is properly adhered, a PTFE (polytetrafluoroethylene) film is then applied to the aluminum surface (Fig. 1(b3)). The PTFE film, known for its excellent triboelectric properties, is placed with precision to ensure full contact with the aluminum layer beneath. Any imperfections during this step could affect the performance of the final device, so this step may also involve additional processes like pressing or controlled heating. Fig. 1(c) depicts the assembly process of the device. Here, the two components are brought together with their respective triboelectric layers (PET and PTFE films) facing each other. This step requires careful alignment to ensure that the patterned surfaces of both components match up perfectly. The components are then pressed together, possibly under controlled pressure conditions, to ensure a strong and consistent interface between the triboelectric layers (Fig. 1(d)). This pressing might involve the use of a jig or fixture to maintain uniform pressure across the entire surface, preventing any areas of weak contact that could diminish the device's performance. The final result is the S-TENG device, where the interaction between the PET and PTFE layers during mechanical deformation generates electricity through the triboelectric effect.

The resultant S-TENG device, as shown in Fig. 1(e), exhibits a compact and flexible form factor, designed to be both mechanically robust and elastically adaptable. The flexibility of the S-TENG device is further demonstrated in Fig. 1(f), where it is shown being bent in various orientations without compromising its structural integrity or functionality. The SEM image in Fig. 1(g) offers a detailed view of the PTFE layer's surface morphology, revealing a finely textured structure with micrometer-scale features. These features are crucial for enhancing the triboelectric effect, thereby improving the overall efficiency of the device.

3.2. The working mechanism of S-TENG device

The operational mechanism of the S-TENG is illustrated in Fig. 2. The S-TENG device operates based on the relative motion between two triboelectric layers: PTFE film and PET film, each backed by a piece of conductive aluminum electrode. The process involves periodic contact and separation, driven by external mechanical stimuli, leading to a continuous generation of electrical power. Fig. 2 (a) depicts the initial state where the PTFE and PET layers are in close contact. During this phase, a static charge is generated due to the triboelectric effect, where electrons transfer from PET (which is more positive in the triboelectric series) to PTFE (more negative). This charge transfer results in an equal and opposite charge distribution on the aluminum electrodes beneath each triboelectric layer. As the external force is removed, the PTFE film and PET film begin to separate (Fig. 2(b)). During this separation, the electrical potential difference between the PET and PTFE layers drives electrons to flow through the external circuit, connected via a load resistor (R). The degree of separation directly affects the magnitude of the induced voltage and the amount of transferred charge. Fig. 2(c) represents the maximum separation state of the S-TENG. In this state, the distance between the PET and PTFE layers is at its peak, maximizing the potential difference and the amount of generated electrical charge. The S-TENG device remains in this state until the external force re-applies, initiating the next contact phase. Upon the reapplication of the external force, the two layers begin to approach each other again (Fig. 2(d)). This re-approach reduces the potential difference, causing the accumulated charges to neutralize as electrons flow back through the external circuit in the opposite direction. This bidirectional flow of electrons results in an alternating current (AC) output. The cyclic process of approaching, pressing, releasing, and separating continuously drives electron flow, enabling the S-TENG

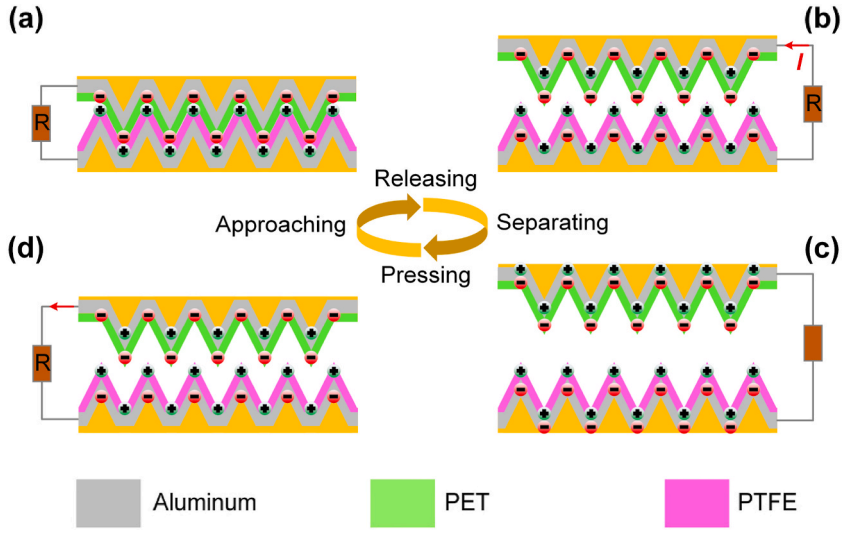

Fig. 2. Operational mechanism of the S-TENG device, including (a) initial state, (b) separation phase, (c) maximum separation state, and (d) re-approaching phase.

to convert mechanical energy into electrical energy efficiently. This principle of operation underpins the potential of S-TENG devices for applications in energy harvesting from ambient mechanical movements, offering a sustainable and flexible power source for various low-power electronic devices.

3.3. The electrical output of S-TENG device

Fig. 3 presents three TENG configurations with varying surface contact structures, alongside their respective output performance metrics in terms of V_{oc}, I_{sc}, and Q_{sc}. According to Fig. 3(b1), Configuration (1) with a flat surface generates a baseline V_{oc} of approximately 59.94 V. Configuration (2), with a single-sided sawtooth structure, shows an increased V_{oc} output of about 80.84 V, attributed to the enhanced surface area and improved contact intimacy. Configuration (3), which utilizes a double-sided sawtooth structure, achieves the highest V_{oc} output of around 98.26 V, indicating the superior performance due to maximum contact area and triboelectric interaction. According to Fig. 3(c), Configuration (1) delivers a baseline I_{sc} of approximately 3.97 μA. Configuration (2) improves the I_{sc} output to around 5.03 μA, demonstrating better charge transfer efficiency. Configuration (3) further enhances the I_{sc} output to about 6.46 μA, correlating with its higher I_{sc} output and improved surface interaction due to the double-sided sawtooth structure. The Q_{sc} in Fig. 3(d) over time for each configuration shows that Configuration (1) generates about 25.94 nC. Configuration (2) increases the charge output to approximately 31.66 nC, while Configuration (3) reaches up to 38.26 nC. These results confirm the significant impact of surface structuring on the charge transfer efficiency of the S-TENG devices. Hence, compared to the flat structure, the serrated structure resulted in a 64 %, 63 %, and 47 % improvement in performance indicators such as V_{oc}, I_{sc}, and Q_{sc} for S-TENG.

To provide a more scientific explanation of the S-TENG's working mechanism, we examined the output characteristics of the TENG from a theoretical perspective. Specifically, in the theoretical framework for the S-TENG, the thicknesses of the two triboelectric layers are denoted by d_1 and d_2. Additionally, the permittivities of the two triboelectric layers and air are represented by ε_1, ε_2, and ε_0, respectively. The area of the frictional surfaces is denoted by S, while the separation distance and transferred charge are indicated as x (t) and Q, respectively. Consequently, the theoretical V-Q-x relationship for the TENG can be expressed as follows:

$$V = -\frac{Q}{S\varepsilon_0}\left(\frac{d_1}{\varepsilon_1}+\frac{d_2}{\varepsilon_2}+x(t)\right)+\frac{\sigma x(t)}{\varepsilon_0} \tag{1}$$

Obviously, as the contact area between the frictional layers increases, the output performance of TENG will also improve. This also demonstrates the scientific nature of S-TENG design from a theoretical perspective. The findings highlight that optimizing the contact surface morphology, especially with sawtooth structures, notably enhances the triboelectric performance of S-TENGs. This enhancement not only boosts energy harvesting efficiency but also underscores the value of S-TENGs in applications related to human posture monitoring, making them a powerful tool for sustainable and flexible energy generation to support low-power electronic devices.

The performance of the S-TENG is critically influenced by the maximum separation distance between the triboelectric materials (PTFE film and PET film) and the bending angle of the device. As described in Fig. 4(a), the V_{oc} of S-TENG is measured for varying separation distances: 1 mm, 2 mm, 3 mm, 5 mm, and 6 mm. The voltage output increases with the separation distance, reaching up to 90.35 V at 6 mm. This trend is attributed to the enhanced potential difference generated as the distance between the triboelectric layers increases, thereby improving the charge transfer efficiency. According to results in Fig. 4(b), the I_{sc} follows a similar trend, increasing

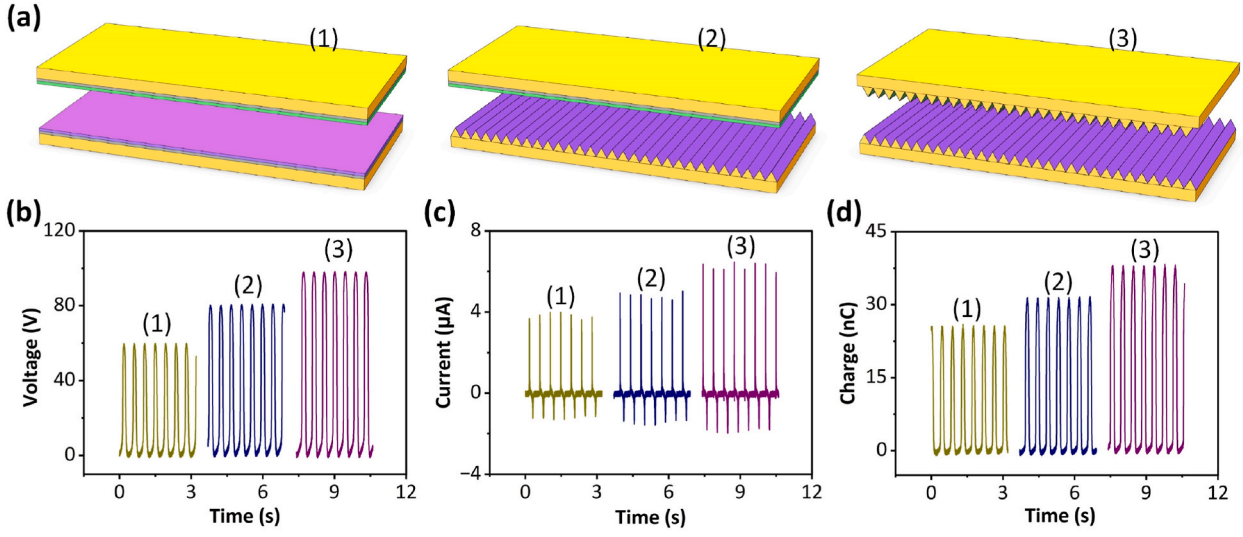

Fig. 3. (a1-a3) The structural diagram of three TENG configurations with different contact structures. The (b) V_{oc}, (c) I_{sc}, and (d) Q_{sc} of three TENG configurations with different contact structures.

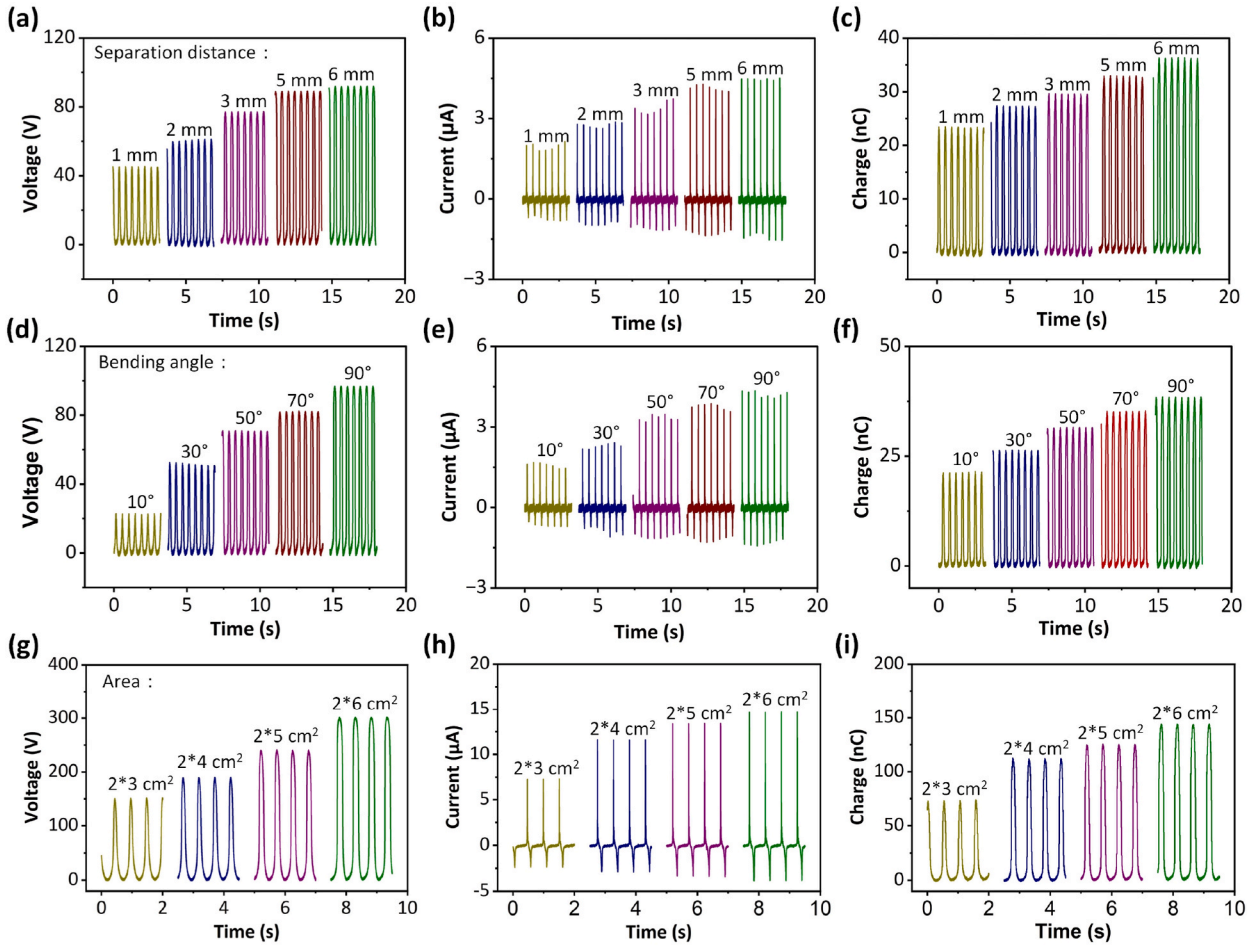

Fig. 4. Effect of separation distance and bending angle on S-TENG output. The (a) V_{oc}, (b) I_{sc}, and (c) Q_{sc} of S-TENG for different separation distances (1 mm, 2 mm, 3 mm, 5 mm, and 6 mm). The (d) V_{oc}, (e) I_{sc}, and (f) Q_{sc} of S-TENG for different bending angles (10°, 30°, 50°, 70°, and 90°). The (g) V_{oc}, (h) I_{sc}, and (i) Q_{sc} of S-TENG with different sizes.

from approximately 2.15 μA at 1 mm to around 4.51 μA at 6 mm. The increase in I_{sc} output with greater separation distances is due to the higher electric field strength, which drives more electrons through the external circuit. The Q_{sc} in Fig. 4(c) also rises with the separation distance, from about 23.51 nC at 1 mm to nearly 36.37 nC at 6 mm. The larger separation distance allows for a greater accumulation of triboelectric charges, resulting in higher Q_{sc}. As shown in Fig. 4(d), the V_{oc} of S-TENG is measured at different bending angles: 10°, 30°, 50°, 70°, and 90°. The voltage increases with the bending angle, reaching up to 98.04 V at 90°. Bending the S-TENG device increases the effective contact area and pressure between the triboelectric layers, thereby enhancing the triboelectric effect. The I_{sc} of S-TENG in Fig. 4(e) also increases with the bending angle, from approximately 1.67 μA at 10° to around 4.35 μA at 90°. The enhanced contact area and pressure improve the charge transfer efficiency, leading to higher current output. Similarly, the Q_{sc} of S-TENG increases with the bending angle, from about 21.54 nC at 10° to nearly 38.51 nC at 90°, as illustrated in Fig. 4(f). The improved contact conditions due to bending result in a greater accumulation and transfer of charges. The results clearly demonstrate that both the separation distance and bending angle significantly impact the S-TENG's output performance. Increasing the separation distance enhances the electric field strength and potential difference, while larger bending angles improve the contact area and pressure between the triboelectric layers. These factors collectively contribute to higher voltage, current, and charge outputs. Optimizing these parameters is essential for maximizing the energy harvesting efficiency of S-TENG devices, making them more effective for practical applications in sustainable and flexible energy generation. Fig. 4(g–i) illustrate the output performance of the S-TENG with varying effective areas. As the area increases from 2×3 cm^2 to 2×6 cm^2, a significant enhancement in the output voltage, current, and charge is observed. Specifically, Fig. 4(g) demonstrates that the output voltage increases proportionally with the effective area, indicating a direct relationship between the area and voltage generation. Similarly, Fig. 4(h) shows an increasing trend in the output current with larger areas, reflecting the capacity of a larger surface area to generate higher current. Furthermore, Fig. 4(i) reveals that the charge output also rises with increasing area, suggesting that a larger area facilitates greater charge accumulation. These results collectively underscore the critical role of the effective area in optimizing the output performance of the S-TENG.

3.4. The sensing application of S-TENG device on swimming training safety monitoring

The contact and separation frequency between the triboelectric layers (PTFE and PET) significantly influence the output of the S-TENG. Fig. 5(a–c) present the V_{oc}, I_{sc}, and Q_{sc} of the S-TENG at varying frequencies (2 Hz, 3 Hz, 4 Hz, and 5 Hz). The V_{oc} of S-TENG maintains stability with frequency, demonstrating higher outputs at increased frequencies, reaching up to 104.94 V at 5 Hz, which indicates that faster contact-separation cycles enhance the charge generation rate, according to results in Fig. 5(a). Similarly, the I_{sc} of S-TENG in Fig. 5(b) shows a positive correlation with frequency, with the current increasing from approximately 5.56 μA at 2 Hz to around 11.78 μA at 5 Hz. The higher frequency enhances the triboelectric effect, resulting in increased I_{sc}. As described in Fig. 5(c), the Q_{sc} of S-TENG exhibits a steady state with frequency, from about 35.68 nC at 2 Hz to nearly 33.64 nC at 5 Hz. As illustrated in Fig. 5(d), the S-TENG demonstrates stability across various humidity levels (20 %, 30 %, 40 %, 50 %, and 60 %), as evidenced by the consistent current outputs. This stability is attributed to the full encapsulation of the device, which protects the triboelectric layers from moisture and ensures reliable performance under different environmental conditions.The S-TENG is evaluated for its potential application in swimming monitoring. Fig. 5(e1, e2) depict swimmers performing backstroke and breaststroke, respectively. The S-TENG is capable of monitoring the swimmer's elbow movements during different strokes, providing real-time data on performance. Fig. 5(f) compares the V_{oc} of S-TENG for small and large elbow swing amplitudes. Larger amplitudes generate higher voltages, indicating that the S-TENG can effectively differentiate between varying movement intensities. Fig. 5(g) shows the V_{oc} for low and high-speed elbow swings. Higher frequencies result in greater voltage outputs, suggesting that the S-TENG can monitor the speed and frequency of swimming strokes accurately. Fig. 5(h) illustrates the potential of the S-TENG for drowning detection. Anomalous voltage patterns indicate irregular movements, which can trigger a drowning warning (as highlighted by the blue box). This feature underscores the S-TENG's capability

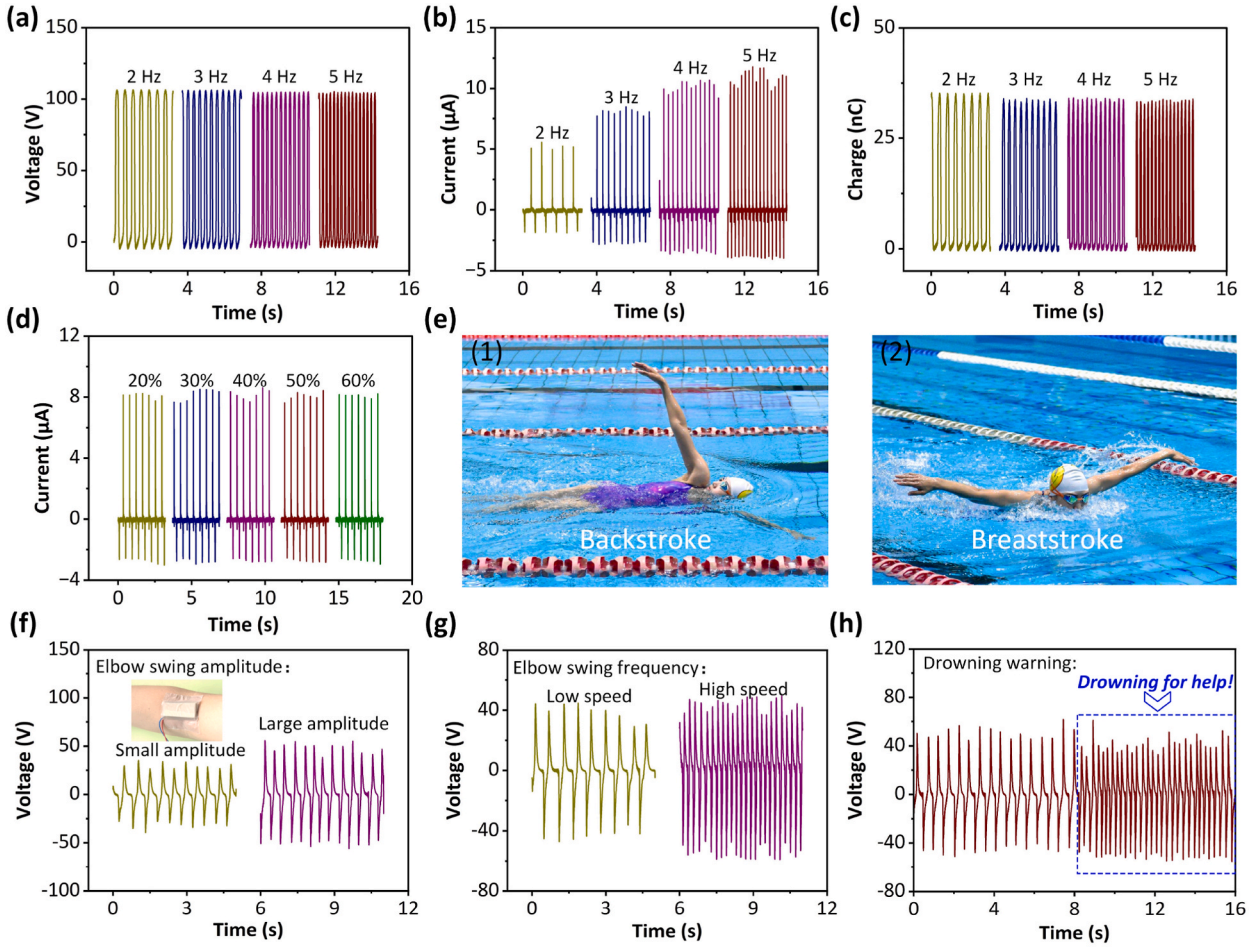

Fig. 5. The (a) V_{oc}, (b) I_{sc}, (c) Q_{sc} of S-TENG at different frequencies (2 Hz, 3 Hz, 4 Hz, 5 Hz) showing increased voltage with higher frequencies. (d) The I_{sc} of S-TENG at various humidity levels (20 %, 30 %, 40 %, 50 %, 60 %), showing stable performance across different environmental conditions. The application of S-TENG in swimming monitoring, such as (e1) backstroke and (e2) breaststroke. (f) The V_{oc} of S-TENG for small and large elbow swing amplitudes, indicating the S-TENG device's capability to detect movement intensity. (g) The V_{oc} of S-TENG for low and high-speed elbow swings, highlighting the S-TENG device's sensitivity to movement frequency. (h) Anomalous voltage patterns triggering a drowning warning, showcasing potential for safety applications in swimming.

to enhance swimmer safety by providing early warnings of distress. The application of S-TENG in swimming monitoring presents a novel approach to tracking and enhancing swimmer performance. The device can accurately measure elbow swing amplitude and frequency, providing valuable data for athletes and coaches. Additionally, the S-TENG's ability to detect irregular movements and potential drowning incidents showcases its potential in safety applications. This excellent design has higher output performance and sensing capability compared to similar TENG structure designs before [50,51]. This study emphasizes the promising potential of combining 3D printing technology with TENG to create customizable, high-performance wearable sensors. Such integration could pave the way for developing highly tailored sensors that meet specific application needs, enhancing both functionality and adaptability in various environments. However, there is still considerable potential for enhancing the selection and design of triboelectric materials. By refining these materials, S-TENG could achieve even higher sensing capabilities. Continued advancements in this area could lead to more precise and efficient performance in various applications.

4. Conclusion

In conclusion, the 3D printed serrated contact structure in S-TENG marks significant advancements in energy harvesting and intelligent motion monitoring. The flexible 3D printing substrate enhances the triboelectric layer's flexibility and ensures more effective contact, leading to improved energy harvesting efficiency. Compared to flat structures, the serrated design resulted in a 64 %, 63 %, and 47 % increase in key performance metrics, including V_{oc}, I_{sc}, and Q_{sc}. Additionally, the serrated contact structure enables S-TENG to function effectively under bending deformation, with Voc, Isc, and Qsc increasing as the bending angle rises, reaching up to 98.04 V, 4.35 μA, and 38.51 nC at a 90° angle. When applied to swimming monitoring, S-TENG not only provides precise data on elbow swing amplitude and frequency but also enhances safety by enabling early detection of distress signals. This study highlights the potential of integrating 3D printing technology with TENG to develop customizable, high-performance wearable sensor. However, there is still significant room for improvement in the selection and design of frictional electrical materials, enabling S-TENG to achieve higher sensing capabilities.

Data availability statements

Data available on request from the authors.

CRediT authorship contribution statement

Jie Gao: Supervision, Software, Funding acquisition, Data curation, Conceptualization. **Wei Wen:** Writing – review & editing, Visualization, Validation, Supervision, Data curation.

Declaration of competing interest

The authors report no conflicts of interest. The authors alone are responsible for the content and writing of this article, the manuscript entitled "A 3D printed serrated contact structure triboelectric nanogenerator for swimming training safety monitoring".

References

[1] H.C. Ates, P.Q. Nguyen, L. Gonzalez-Macia, et al., End-to-end design of wearable sensors[J], Nat. Rev. Mater. 7 (11) (2022) 887–907.
[2] R. Yin, D. Wang, S. Zhao, et al., Wearable sensors-enabled human–machine interaction systems: from design to application[J], Adv. Funct. Mater. 31 (11) (2021) 2008936.
[4] A Haroun, M Tarek, M Mosleh, et al., Recent Progress on Triboelectric Nanogenerators for Vibration Energy Harvesting and Vibration Sensing, Nanomaterials (Basel) 12 (17) (2022).
[3] S.D. Mamdiwar, Z. Shakruwala, U. Chadha, et al., Recent advances on IoT-assisted wearable sensor systems for healthcare monitoring[J], Biosensors 11 (10) (2021) 372.
[5] W. Qiao, L. Zhou, Z. Zhao, et al., A self-powered vector motion sensor for smart robotics and personalized medical rehabilitation[J], Nano Energy 104 (2022) 107936.
[6] Quan Zhang, et al., Wearable triboelectric sensors enabled gait analysis and waist motion capture for IoT-based smart healthcare applications[J], Adv. Sci. 9 (4) (2022) 2103694.
[7] Quan Zhang, et al., Wearable triboelectric sensors enabled gait analysis and waist motion capture for IoT-based smart healthcare applications, Adv. Sci. 9 (4) (2022) 2103694.
[8] J. Wang, Z. Wang, F. Gao, et al., Swimming stroke phase segmentation based on wearable motion capture technique[J], IEEE Trans. Instrum. Meas. 69 (10) (2020) 8526–8538.
[9] W.G. Kim, D.W. Kim, I.W. Tcho, et al., Triboelectric nanogenerator: structure, mechanism, and applications[J], ACS Nano 15 (1) (2021) 258–287.
[10] H. Wang, M. Han, Y. Song, et al., Design, manufacturing and applications of wearable triboelectric nanogenerators[J], Nano Energy 81 (2021) 105627.
[11] S. Jang, H. Kim, J.H. Oh, Simple and rapid fabrication of pencil-on-paper triboelectric nanogenerators with enhanced electrical performance[J], Nanoscale 9 (35) (2017) 13034–13041.
[12] X. Wang, S. Niu, Y. Yin, et al., Triboelectric nanogenerator based on fully enclosed rolling spherical structure for harvesting low-frequency water wave energy [J], Adv. Energy Mater. 5 (24) (2015) 1501467.
[13] X.W. Zhang, G.Z. Li, G.G. Wang, et al., High-performance triboelectric nanogenerator with double-surface shape-complementary microstructures prepared by using simple sandpaper templates[J], ACS Sustain. Chem. Eng. 6 (2) (2018) 2283–2291.
[14] P. Bai, G. Zhu, Z.H. Lin, et al., Integrated multilayered triboelectric nanogenerator for harvesting biomechanical energy from human motions[J], ACS Nano 7 (4) (2013) 3713–3719.
[15] M. Yin, X. Lu, G. Qiao, et al., Mechanical regulation triboelectric nanogenerator with controllable output performance for random energy harvesting[J], Adv. Energy Mater. 10 (22) (2020) 2000627.

[16] Z. Niu, W. Cheng, M. Cao, et al., Recent advances in cellulose-based flexible triboelectric nanogenerators[J], Nano Energy 87 (2021) 106175.
[17] Y. Dong, S.S.K. Mallineni, K. Maleski, et al., Metallic MXenes: a new family of materials for flexible triboelectric nanogenerators[J], Nano Energy 44 (2018) 103–110.
[18] Y. Li, Z. Zhao, Y. Gao, et al., Low-cost, environmentally friendly, and high-performance triboelectric nanogenerator based on a common waste material[J], ACS Appl. Mater. Interfaces 13 (26) (2021) 30776–30784.
[19] P. Supraja, R.R. Kumar, S. Mishra, et al., A simple and low-cost triboelectric nanogenerator based on two dimensional ZnO nanosheets and its application in portable electronics[J], Sensor Actuator Phys. 335 (2022) 113368.
[20] S. Hu, J. Weber, S. Chang, et al., A low-cost simple sliding triboelectric nanogenerator for harvesting energy from human activities[J], Advanced Materials Technologies 7 (9) (2022) 2200186.
[21] Yuanming Zeng, et al., Flexible triboelectric nanogenerator for human motion tracking and gesture recognition[J], Nano Energy 91 (2022) 106601.
[22] S. An, X. Pu, S. Zhou, et al., Deep learning enabled neck motion detection using a triboelectric nanogenerator[J], ACS Nano 16 (6) (2022) 9359–9367.
[23] M.S. Rasel, P. Maharjan, M. Salauddin, et al., An impedance tunable and highly efficient triboelectric nanogenerator for large-scale, ultra-sensitive pressure sensing applications[J], Nano Energy 49 (2018) 603–613.
[24] F.R. Fan, L. Lin, G. Zhu, et al., Transparent triboelectric nanogenerators and self-powered pressure sensors based on micropatterned plastic films[J], Nano Lett. 12 (6) (2012) 3109–3114.
[25] S.B. Jeon, Y.H. Nho, S.J. Park, et al., Self-powered fall detection system using pressure sensing triboelectric nanogenerators[J], Nano Energy 41 (2017) 139–147.
[26] I. Mehamud, P. Marklund, M. Björling, et al., Machine condition monitoring enabled by broad range vibration frequency detecting triboelectric nano-generator (TENG)-based vibration sensors[J], Nano Energy 98 (2022) 107292.
[27] Z. Lin, C. Sun, G. Zhang, et al., Flexible triboelectric nanogenerator toward ultrahigh-frequency vibration sensing[J], Nano Res. 15 (8) (2022) 7484–7491.
[28] F. Sun, Y. Zhu, C. Jia, et al., Advances in self-powered sports monitoring sensors based on triboelectric nanogenerators[J], J. Energy Chem. 79 (2023) 477–488.
[29] J. Luo, W. Gao, Z.L. Wang, The triboelectric nanogenerator as an innovative technology toward intelligent sports[J], Adv. Mater. 33 (17) (2021) 2004178.
[30] C. Li, Y. Zhu, F. Sun, et al., Research progress on triboelectric nanogenerator for sports applications[J], Energies 15 (16) (2022) 5807.
[31] Y. Kang, B. Wang, S. Dai, et al., Folded elastic strip-based triboelectric nanogenerator for harvesting human motion energy for multiple applications[J], ACS Appl. Mater. Interfaces 7 (36) (2015) 20469–20476.
[32] K. Xia, Z. Zhu, H. Zhang, et al., Painting a high-output triboelectric nanogenerator on paper for harvesting energy from human body motion[J], Nano Energy 50 (2018) 571–580.
[33] J. Liao, Y. Zou, D. Jiang, et al., Nestable arched triboelectric nanogenerator for large deflection biomechanical sensing and energy harvesting[J], Nano Energy 69 (2020) 104417.
[34] J. Ren, C. Gao, J. An, et al., Arc-shaped triboelec[J]tric nanogenerator based on rolling structure for harvesting low-frequency water wave energy, Advanced Materials Technologies 6 (11) (2021) 2100359.
[35] K. Xia, Z. Zhu, J. Fu, et al., Multifunctional conductive copper tape-based triboelectric nanogenerator and as a self-powered humidity sensor[J], IEEE Trans. Electron. Dev. 66 (6) (2019) 2741–2745.
[36] W. Wang, A. Yu, X. Liu, et al., Large-scale fabrication of robust textile triboelectric nanogenerators[J], Nano Energy 71 (2020) 104605.
[37] K. Xia, D. Wu, J. Fu, et al., A high-output triboelectric nanogenerator based on nickel–copper bimetallic hydroxide nanowrinkles for self-powered wearable electronics[J], J. Mater. Chem. A 8 (48) (2020) 25995–26003.
[38] W. Xu, L.B. Huang, M.C. Wong, et al., Environmentally friendly hydrogel-based triboelectric nanogenerators for versatile energy harvesting and self-powered sensors[J], Adv. Energy Mater. 7 (1) (2017) 1601529.
[39] F.G. Torres, O.P. Troncoso, G.E. De-la-Torre, Hydrogel-based triboelectric nanogenerators: properties, performance, and applications[J], Int. J. Energy Res. 46 (5) (2022) 5603–5624.
[40] X. Luo, L. Zhu, Y.C. Wang, et al., A flexible multifunctional triboelectric nanogenerator based on MXene/PVA hydrogel[J], Adv. Funct. Mater. 31 (38) (2021) 2104928.
[41] Y. Yang, X.J. Hou, W.P. Geng, et al., Human movement monitoring and behavior recognition for intelligent sports using customizable and flexible triboelectric nanogenerator[J], Sci. China Technol. Sci. 65 (4) (2022) 826–836.
[42] G. Khandelwal, N.P.M.J. Raj, S.J. Kim, Triboelectric nanogenerator for healthcare and biomedical applications[J], Nano Today 33 (2020) 100882.
[43] R. Li, X. Wei, J. Xu, et al., Smart wearable sensors based on triboelectric nanogenerator for personal healthcare monitoring[J], Micromachines 12 (4) (2021) 352.
[44] Z. Liu, H. Li, B. Shi, et al., Wearable and implantable triboelectric nanogenerators[J], Adv. Funct. Mater. 29 (20) (2019) 1808820.
[45] C. Ning, L. Tian, X. Zhao, et al., Washable textile-structured single-electrode triboelectric nanogenerator for self-powered wearable electronics[J], J. Mater. Chem. A 6 (39) (2018) 19143–19150.
[46] B. Chen, W. Tang, T. Jiang, et al., Three-dimensional ultraflexible triboelectric nanogenerator made by 3D printing[J], Nano Energy 45 (2018) 380–389.
[47] B. Chen, W. Tang, Z.L. Wang, Advanced 3D printing-based triboelectric nanogenerator for mechanical energy harvesting and self-powered sensing[J], Mater. Today 50 (2021) 224–238.
[48] H. Qiao, Y. Zhang, Z. Huang, et al., 3D printing individualized triboelectric nanogenerator with macro-pattern[J], Nano Energy 50 (2018) 126–132.
[49] F. Peng, M. Gao, Z. Han, et al., One-step fabrication of sandwiched film based triboelectric nanogenerator for large-area energy harvester and precise self-powered sensor[J], Nano Energy 103 (2022) 107771.
[50] Z. Wang, W. Gao, A wave structure triboelectric nanogenerator for race walking motion sensing[J], Mater. Technol. 37 (13) (2022) 2637–2643.
[51] Z. Wang, Z. Liu, Y. Wang, et al., A flexible triboelectric nanogenerator based on wave structure PDMS for joint monitoring in basketball training[J], AIP Adv. 13 (12) (2023).